Optics & Laser Technology 171 (2024) 110389

Contents lists available at ScienceDirect

Optics and Laser Technology

journal homepage: www.elsevier.com/locate/optlastec

Full length article

Holographic silver nanograting formation driven by TE_0, TE_1, and TE_2 mode propagation in an AgCl slab Waveguide: Optical properties and analysis

Razieh Talebi [a,b,*], Daryoosh Vashaee [c,d]

[a] Department of Physics, University of Isfahan, Isfahan 81746, Iran
[b] Quantum Optics Group, Department of Physics, University of Isfahan, Isfahan 81746, Iran
[c] Department of Electrical and Computer Engineering, North Carolina State University, Raleigh, NC 27606, USA
[d] Department of Materials Science and Engineering, North Carolina State University, Raleigh, NC 27606, USA

ARTICLE INFO

Keywords:
Holographic silver nanogratings
AgCl thin film
linear dichroism
birefringence
anisotropic nanostructures
Diffraction

ABSTRACT

Holographic silver nanogratings on the surface and within the volume, which have significant potential for data storage applications, are generated in silver chloride (AgCl) waveguides using a single laser beam exposure. This formation process leverages the interference between the polarized incident wave and the TE_m modes propagating inside the AgCl waveguide. These plasmonic nanogratings are anisotropic nanostructures, demonstrating intriguing optical traits such as wavelength-specific linear dichroism and birefringence. The observed linear dichroism and birefringence in the holographic silver nanograting can modify the optical rotation and ellipticity of a probe beam traversing this anisotropic medium. Notably, volume holographic nanogratings function as complex nanogratings with a periodicity exceeding that of the incident wavelength. As a result, upon exposure, these complex nanogratings exhibit discernible light diffraction, while the surface holographic nanogratings do not show any diffraction pattern. Additionally, as the AgCl film thickness is increased and more complex nanogratings are formed within the AgCl waveguides, there is a noted reduction in the resulting birefringence.

1. Introduction

Silver chloride (AgCl) films, when deposited on glass substrates, establish asymmetric waveguides. The number of modes that can be coupled into these AgCl waveguides directly correlates with the thickness of the AgCl film. By depositing silver nanoparticles (Ag NPs) onto an AgCl film (Ag-AgCl), the film transforms into a light-sensitive plasmonic material receptive to visible light. Furthermore, the presence of these silver nanoparticles facilitates the easy coupling of an incident light beam into the AgCl waveguide, eliminating the need for specialized couplers like prisms. As the incident wave interferes with the propagating wave within the AgCl waveguide, it results in the formation of periodic silver chain-like structures, known as silver nanogratings, within the AgCl film [1,2].

In thinner AgCl waveguides, only the TE_0 mode can propagate. Thus, when a linearly polarized laser beam irradiates such a sample, a surface silver nanograting manifests within the AgCl thin film. In these sub-wavelength Ag-AgCl thin films, attributes of the incident light beam, such as polarization state, incident angle, and light wavelength, can be captured and recorded [3–7]. As the AgCl film's thickness increases up to a thickness comparable to the wavelength of incident light beam, higher-order TE modes can also be channeled within the AgCl waveguide [1,8]. Under these conditions, the periodic silver structures generated within the AgCl waveguide diverge from the previously researched surface silver nanogratings [4–7], functioning instead as volume holographic silver nanogratings.

These volume holographic nanogratings boast a range of optical applications, including data storage, spatial-spectral filters, and serving as couplers in waveguide-driven display systems [9–11]. An advantage of employing the Ag-AgCl thin film as a recording medium is its straightforward fabrication process, enabling the easy formation of volume holographic nanogratings within this medium. A singular low-power polarized laser beam suffices to create a volume silver nanograting in the AgCl thin film [1,3–8].

Silver nanogratings within AgCl films are inherently anisotropic plasmonic nanostructures, with their optical responses being contingent

* Corresponding author.
E-mail address: r.talebi@sci.ui.ac.ir (R. Talebi).

https://doi.org/10.1016/j.optlastec.2023.110389
Received 6 September 2023; Received in revised form 4 November 2023; Accepted 23 November 2023
Available online 30 November 2023

on the probe beam's polarization direction [7,12]. Given that these anisotropic plasmonic nanostructures are sensitive to light polarization, they hold potential in applications such as optical polarizers and sensors [13,14]. Linear dichroism (LD) and birefringence stand out as significant properties of these anisotropic nanostructures. In the context of the Ag-AgCl thin film, such attributes have been exclusively measured for samples that contain silver nanogratings in an AgCl waveguide with a cutoff thickness TE_0 mode [7,12]. Yet, linear dichroism and birefringence haven't been evaluated for volume holographic silver nanogratings in AgCl waveguides that propagate higher-order TE modes.

Linear dichroism in an anisotropic medium results in the polarization azimuth of the probe beam undergoing rotation as it traverses this medium. On the other hand, the birefringence of an anisotropic medium can be discerned by assessing the ellipticity angle of the probe beam as it moves through the medium. The maximal absolute values of both linear dichroism and birefringence in these anisotropic plasmonic nanostructures are influenced by the wavelength of the localized surface plasmon resonance (LSPR) of silver nanoparticles [7,12,14]. Additionally, the thickness of the anisotropic medium plays a role in determining its optical rotation and ellipticity [8,14]. As such, in this paper, we examine the influence of AgCl thickness on the linear dichroism and birefringence of these anisotropic nanostructures.

In our study, we fabricated both surface and volume silver nanogratings, leveraging the interference between the incident laser beam and the TE_m modes propagating in the AgCl film. As the AgCl film's thickness was augmented, a greater number of TE_m modes were able to couple into the AgCl waveguide, leading to increasingly intricate interference patterns within the film. The linear dichroism and birefringence observed in AgCl films of varied thicknesses were subsequently measured and contrasted.

2. Materials and methods

In this section, we detail both the sample preparation process and the theoretical framework employed to elucidate the propagation of TE_m modes in an asymmetrical AgCl waveguide when irradiated by a single laser beam.

2.1. Sample preparation

Ag-AgCl films were fabricated employing a two-step sequential thermal evaporation technique. This method was chosen for its effectiveness in producing films with the desired properties, and it was executed on a pristine microscope glass slide under vacuum conditions maintained at a pressure of 5×10^{-5} mbar. The fabrication process commenced with the deposition of an AgCl thin film onto the glass substrate. Notably, AgCl films do not inherently absorb light in the visible spectrum [15]. However, when exposed to light irradiation, the AgCl film undergoes transformation with the formation of silver nanoparticles. This induces specific optical phenomena, notably the Weigert effect and the activation of surface-enhanced Raman scattering (SERS) [1,16].

For advancing the visible-light responsiveness of AgCl, especially to harness its potential in applications like photocatalytic performance, multicolor photochromic responses, and spontaneous periodic structure formation, an additional layer of silver nanoparticles becomes imperative [1,15,17]. Consequently, a silver layer of 10 ± 2 nm was thermally evaporated onto the AgCl film. It is crucial to understand that this silver layer is not a continuous film. Instead, it presents itself as a granulated layer, composed of sporadic silver nanoparticles that are interspersed across the AgCl film.

For the scope of this paper, we focused on exploring the propagation of TE_0, TE_1, and TE_2 modes in AgCl waveguides of varying thicknesses. To this end, we prepared three distinct Ag-AgCl films, each varying in AgCl thickness. To ascertain the optimal cutoff thickness required for the propagation of TE_m modes in the AgCl waveguide, we employed the subsequent equation [2]:

$$h_m = \frac{\lambda_0}{2\pi\sqrt{n_f^2 - n_s^2}}\left(m\pi + \arctan\sqrt{\frac{n_s^2 - n_0^2}{n_f^2 - n_s^2}}\right), \quad (1)$$

Here, m denotes the integer index indicative of the order of TE modes progressing within the AgCl waveguide. $\lambda = 532$ nm represents the wavelength of the incident laser beam. The refractive index of the AgCl film is captured by $n_f = 2.06$ [8], while $n_s = 1.52$ stands for the refractive index of the glass substrate at a wavelength $\lambda_0 = 532$ nm. Lastly, n_0=1 signifies the refractive index of air that envelops the AgCl waveguide.

From the calculations, the cutoff thicknesses deduced for the TE_0, TE_1, and TE_2 modes are $h_0 \approx 43$ nm, $h_1 \approx 236$ nm, and $h_2 \approx 429$ nm, respectively. Hence, we categorize the Ag-AgCl samples as:

- Type I for samples Ag(10 nm)-AgCl ($h_0 \approx 43$ nm)
- Type II for samples Ag(10 nm)-AgCl ($h_1 \approx 236$ nm)
- Type III for samples Ag(10 nm)-AgCl ($h_2 \approx 429$ nm)

2.2. Sample irradiation

All variants of the Ag-AgCl films on the glass substrate underwent irradiation from a continuous-wave (cw) Nd:YAG laser with a wavelength $\lambda = 532$ nm, spanning a duration of 15 min. As depicted in Fig. 1 (a), the normally incident laser beam is directed towards the negative z-axis, with the beam being linearly polarized along the y-axis. This polarization is mathematically expressed as:

$$E_{i,y} = E_0\cos(k_0 z). \quad (2)$$

In this equation, E_0 denotes the amplitude of the incident beam, while $k_0 = 2\pi/\lambda_0$ is its wavenumber. The power of this incident laser beam is roughly set to 50 mW. Owing to Rayleigh scattering [18], the silver nanoparticles disperse a fraction of the incident laser beams. A segment of these scattered beams, which satisfy the total reflection condition, are permitted to traverse the AgCl waveguide. The constructive interference of the beam traversing within the AgCl waveguide and the incident beam crafts bright and dark fringes on the AgCl thin film, as illustrated

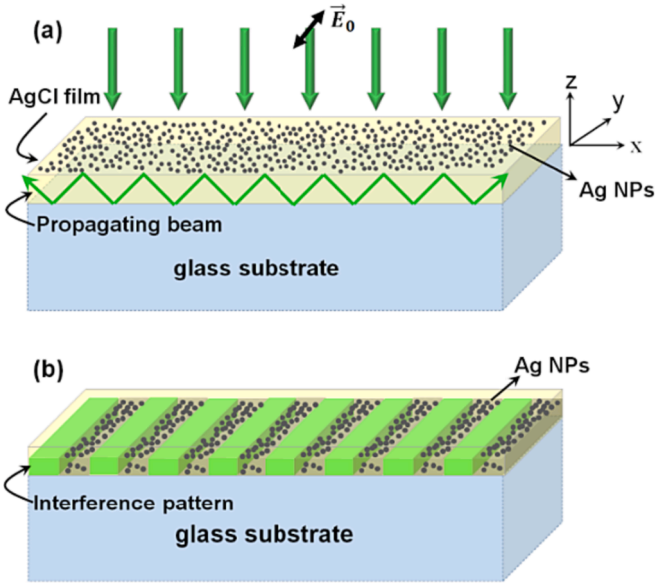

Fig. 1. A graphical representation illustrating the Ag-AgCl film mounted on a glass substrate: (a) depicts the film when exposed to a normally incident, linearly polarized laser beam; (b) highlights the accumulation of silver nanoparticles in a chain-like formation, particularly within the dark fringes resulting from the interference pattern.

in Fig. 1(b). Notably, under the influence of this interference pattern, the silver nanoparticles tend to gravitate towards the dark fringes [19].

During irradiation with a normal incidence, the spatial separation between every two dark fringes of the interference pattern, held constant at a specific value of z (z = cte), is dictated by the subsequent relationship [19]:

$$d = \frac{\lambda_0}{n_{\text{eff}}(z)}. \tag{3}$$

Within this equation, n_{eff} (z) symbolizes the effective refractive index of the AgCl waveguide at the point where the coupling mode is in progression. This effective refractive index sits between the refractive indices of the glass substrate and the AgCl film, meaning $n_s < n_{\text{eff}} < n_f$.

As detailed in Section 2.1, the thickness of the AgCl film determines which modes can propagate within the film. In Fig. 2, three distinct thicknesses of AgCl films are presented. The electric field of the mode propagated within the AgCl film can be represented as [2]:

$$E_y = E_f \cos[\kappa_f z - \phi_s], \tag{4}$$

Here, E_f is the amplitude of the electric field, κ_f is the transverse propagation constant, and ϕ_s represents the phase shift upon reflection from the AgCl-glass boundary. The transverse propagation constant is further defined by [2]:

$$\kappa_f = \sqrt{n_f^2 k_0^2 - \beta^2}, \tag{5}$$

Where $\beta = n_{\text{eff}}\, k_0$ is the propagation constant. By enforcing boundary conditions at both the AgCl-air and AgCl-glass interfaces, we derive the subsequent phase shifts [2]:

$$\phi_c = \arctan\frac{\gamma_c}{\kappa_f}, \tag{6}$$

$$\phi_s = \arctan\frac{\gamma_s}{\kappa_f}. \tag{7}$$

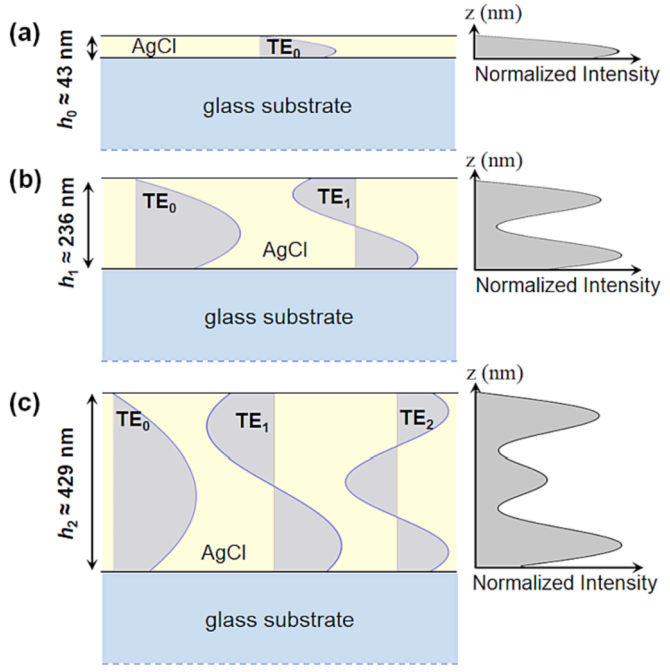

Fig. 2. Electric field distribution of propagated modes and their normalized intensities within the AgCl waveguide for different thicknesses: (a) $h_0 \approx 43$ nm (sample type I), (b) $h_1 \approx 236$ nm (sample type II), and (c) $h_2 \approx 429$ nm (sample type III).

Here, $\gamma_c = \sqrt{\beta^2 - n_c^2 k_0^2}$ and $\gamma_s = \sqrt{\beta^2 - n_s^2 k_0^2}$ respectively correspond to transverse decay at the AgCl-air and AgCl-glass interfaces. The collective phase shifts within the AgCl asymmetrical waveguide must equate to an integer multiple of 2π, a criterion termed the transverse resonance condition, represented by [2]:

$$2\kappa_f h_m - 2\phi_c - 2\phi_s = m2\pi. \tag{8}$$

In this equation, $-2\phi_c$ and $-2\phi_s$ are respectively the phase shifts upon total reflection from the AgCl-air and AgCl-glass interfaces. By inserting κ_f from Equation (8) into Equation (4), we obtain the distribution of the electric field for propagated modes in asymmetric waveguides. Fig. 2(a), 2(b), and 2(c) illustrate the distribution of the electric field traversing through AgCl asymmetrical waveguides with thicknesses of 43 nm, 236 nm, and 429 nm, respectively.

As illustrated in Fig. 2, the 43 nm-thick AgCl waveguide supports only the TE_0 mode. In contrast, the 236 nm-thick AgCl waveguide accommodates both TE_0 and TE_1 modes, while the 429 nm-thick AgCl waveguide can propagate TE_0, TE_1, and TE_2 modes. The intensity of modes propagated within the AgCl waveguide is given by:

$$I = \sum_m |E_{y,m}|^2, \tag{9}$$

where $E_{y,m}$ is the electric field of the m^{th} propagated mode in the AgCl waveguide, as derived from equation (4). Fig. 2 presents the normalized intensity distribution of the propagating wave at different depths (z) within the AgCl waveguide. The interference pattern's visibility in Fig. 1 (b) is at its peak where the propagated wave's intensity within the AgCl waveguide reaches its maximum. Notably, the intensity distributions shown in Fig. 2(b) and 2(c) exhibit two and three peaks, respectively. This suggests that multiple interference patterns with high visibility are likely to form at different depths within these samples.

Fig. 3 illustrates the apparatus employed to fabricate silver nanogratings within the AgCl waveguide. The laser beam, boasting a 2.7 mm diameter, is oriented towards the negative z-axis. This beam, once it traverses the Glan–Taylor polarizer, achieves linear polarization along the y-axis ($\vec{E}$). Positioned between the sample and the polarizer is a screen, uniquely characterized by its central aperture with a diameter of 5.8 mm.

This setup allows for the observation of silver nanogratings in the sample by monitoring the back-scattering and reflective diffraction patterns on the screen during laser beam irradiation [19].

Silver nanogratings' formation in an AgCl film results in an anisotropic plasmonic medium. The optical behaviour of this medium can be examined through absorption measurements [12,18]. For this, a UV–vis JASCO V-670 spectrophotometer was utilized. The optical density, a measure of absorption, for irradiated Ag-AgCl samples is defined as [12,18]:

$$OD = -\log(\frac{T}{T_0}), \tag{10}$$

where T represents the irradiated samples' transmission and T_0 is that of unaltered glass.

For assessing the anisotropy of the plasmonic medium, a linearly polarized probe beam measures the optical density. The discrepancy in optical density across two perpendicular directions of the sample is termed linear dichroism, given as [12,20]:

$$LD = OD\| - OD_\perp. \tag{11}$$

Here, $OD\|$ and $OD_\perp$ represent the optical densities as measured by the polarized probe beam aligned with and perpendicular to the grating lines, respectively.

An anisotropic medium possesses the unique property of rotating the azimuth of light polarization. This characteristic rotation in polarization

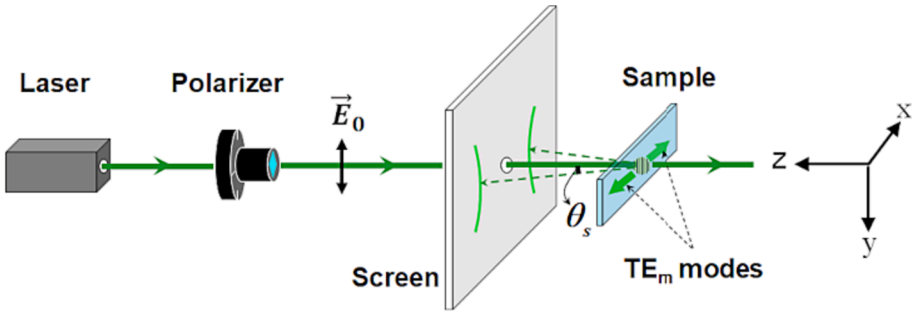

Fig. 3. Schematic illustration of the irradiation setup employed to produce silver nanogratings, with simultaneous monitoring of scattering and diffraction patterns.

within the medium is termed optical rotation (OR). Notably, the extent of this optical rotation varies depending on the orientation of the sample within the medium. The mathematical relationship expressing optical rotation as a function of sample orientation, Φ, is given by [7,14,21]:

$$OR = A_0 \sin(2\Phi). \quad (12)$$

In this equation, A_0 represents the amplitude of the sine function, which correlates with the linear dichroism inherent in the anisotropic medium. Importantly, A_0 is also directly proportional to the medium's thickness [7,14].

Birefringence is another characteristic of anisotropic media, leading

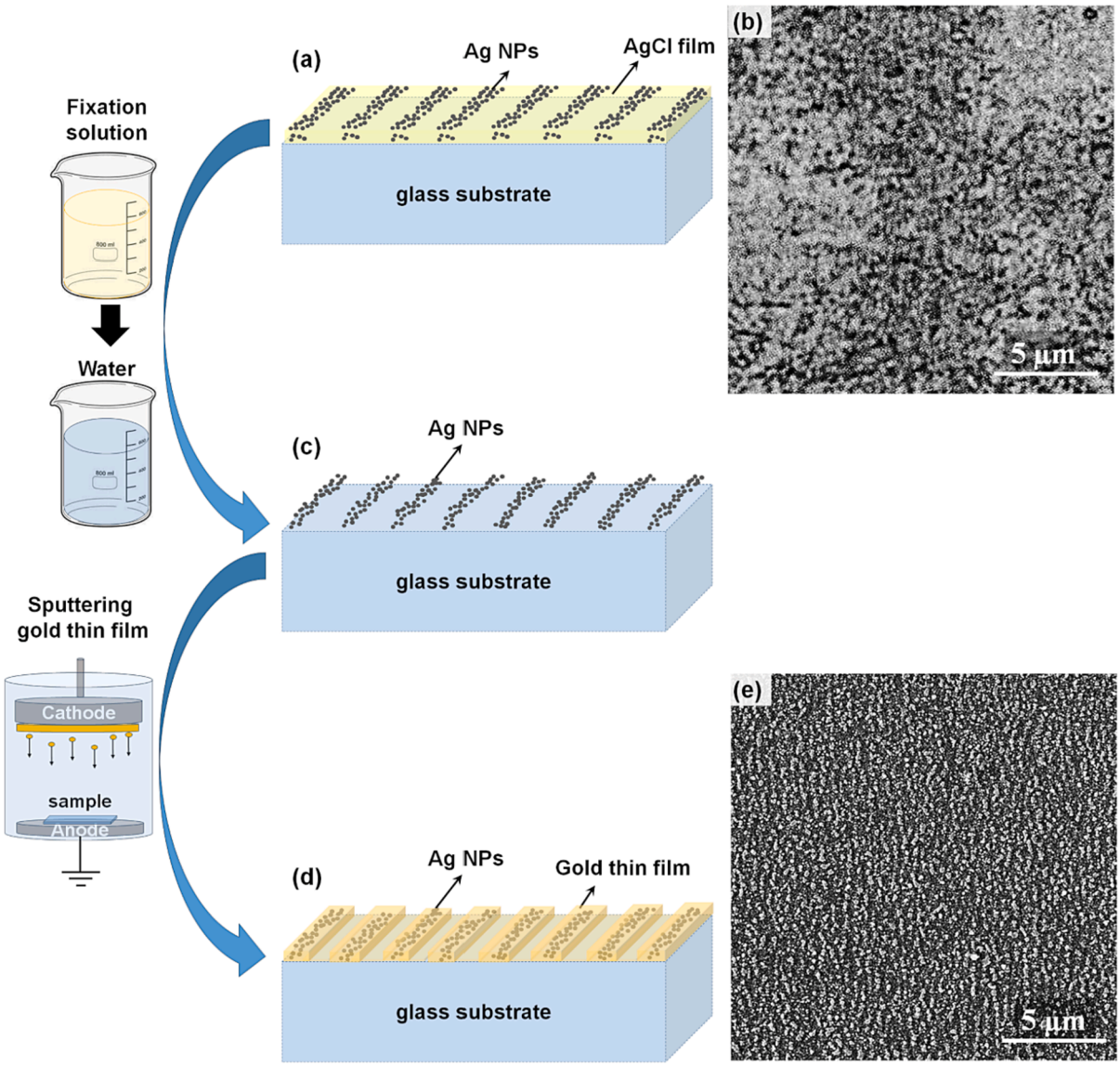

Fig. 4. Process for preparing the irradiated Ag-AgCl sample for SEM imaging. (a) Ag-AgCl film post-laser irradiation, (b) Confocal Laser Scanning Microscope capture of the Ag-AgCl surface, (c) surface rinsing using fixation solution and water, (d) applying a thin gold film to the cleaned sample, and (e) SEM image of the resultant silver nanograting.

to ellipticity when a linear probe beam passes through it. The relationship between ellipticity and sample orientation can be described as [7,21]:

$$\eta = A_1 \sin(2\Phi). \tag{13}$$

Wherein A_1 is the amplitude of the sine function and is defined by [7,21]:

$$A_1 = \frac{\pi h}{\lambda} \Delta n. \tag{14}$$

Here, λ represents the probe beam's wavelength, h is the thickness of the anisotropic medium, and Δn is the birefringence induced in the medium.

3. Results and discussion

3.1. Analysis of the scattering pattern

After the laser irradiation, we examine the sample's morphology using scanning electron microscopy. Due to the intricate volume structures of the holographic silver nanograting in the AgCl thin film, preparing the samples for scanning is essential. Fig. 4 outlines this preparation process.

Fig. 4(a) illustrates the formation of silver nanogratings within the AgCl film post-laser irradiation. The surface of the post-irradiated Ag-AgCl film is captured in Fig. 4(b) using a Confocal Laser Scanning Microscope (Keyence VKx1100). Given the historical use of AgCl film in photographic film and paper, its unique properties are beneficial. Specifically, AgCl can dissolve in photographic film's fixation solution without affecting silver nanoparticles. Utilizing this property, the Ag-AgCl film's surface is rinsed with the fixation solution and subsequently with water, ensuring only the silver nanoparticles are left behind, as depicted in Fig. 4(c). For SEM imaging, the sample is first coated with a 30 nm-thick gold layer using the sputtering deposition process. This gold coating ensures surface conductivity without altering the sample's morphology, as depicted in Fig. 4(d). Once prepared, high-resolution SEM images are captured using the Tescan Mira3 FESEM. Fig. 4(e) displays the resulting SEM image, highlighting regions of aggregated silver nanoparticles. These regions appear brighter and exhibit a bumpy surface texture, signaling areas with a concentration of silver nanoparticles. Although these SEM images are of high resolution, the periodicity of the nanogratings is best discerned using the Fast Fourier Transform (FFT) feature in the Gwyddion software.

As demonstrated in Figure 5(a), the scattering pattern for sample type I exhibits a candle flame-like shape oriented in the direction of light polarization $(\vec{E}_0)$. This is further clarified in Figure 5(d), where the alignment of silver nanoparticles in the $(\vec{E}_0)$ direction, leading to the formation of surface silver nanogratings in sample type I, is evident. The inset of Figure 5(d) displays the FFT feature of the SEM image. The presence of symmetrical, sickle-shaped lines in the FFT suggests the establishment of a periodic nanostructure. Given that the silver chains have a somewhat wavy morphology rather than being perfectly straight, the FFT yields curved lines instead of distinct dots. The FFT also helps in determining the spacing between the lines of the silver nanogratings. For sample type I, this spacing is approximately 347 ± 2 nm. Consequently, by applying equation (3), an effective refractive index of 1.53 is deduced.

Turning our attention to sample type II, Figure 5(b) reveals a prominent central scattering line flanked by two symmetrical curved lines. The SEM image of this sample, presented in Figure 5(e), indicates that the alignment of silver nanoparticles in sample type II is less orderly than in sample type I. The FFT of this SEM image reveals two pairs of lines, suggesting the existence of two distinct silver nanogratings with different spacings. The measured spacings for these nanogratings are 310 nm ± 2 nm and 345 nm ± 2 nm, yielding effective refractive indices of 1.72 and 1.54, respectively. These varying refractive indices suggest

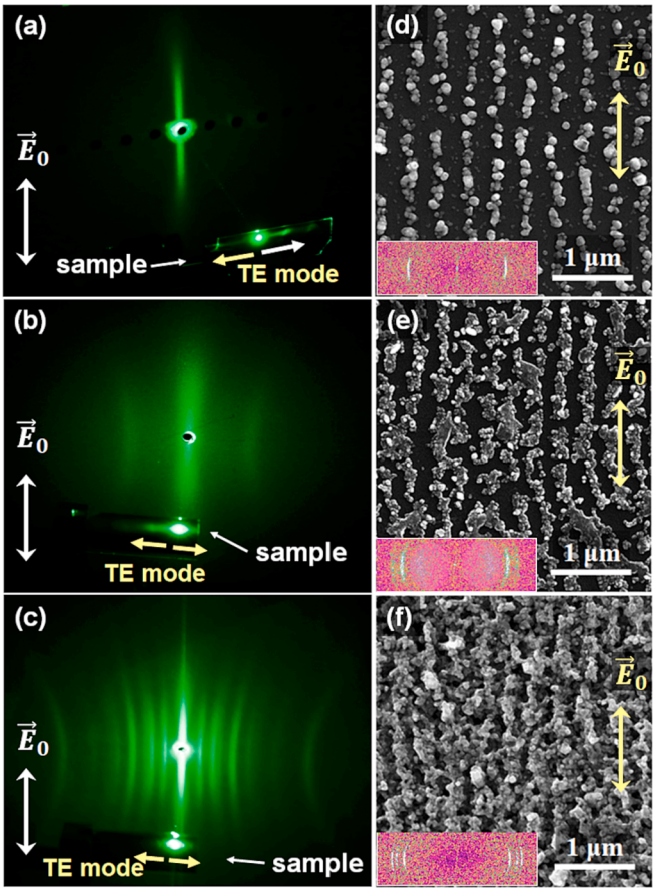

Fig. 5. Scattering patterns for samples are presented as follows: (a) type I, (b) type II, and (c) type III. The associated SEM images, along with their respective FFT features, are depicted in (d) for type I, (e) for type II, and (f) for type III.

that silver nanogratings have formed at different depths within the AgCl thin film. Based on the distinctive diffraction patterns observed and the variation in the effective refractive index at different depths of the AgCl film, it can be inferred that a volume holographic nanograting is formed in sample type II.

For sample type III, Figure 5(c) reveals six symmetric pairs of curved lines surrounding the central scatter line on the display. The presence of three pairs of lines in the FFT feature, seen in the inset of Figure 5(f), indicates the formation of three distinct silver nanogratings. These have line-spaces of 270 nm ± 2 nm, 300 nm ± 2 nm, and 330 nm ± 2 nm and are established at varying depths within the AgCl film. Their respective effective refractive indices are 1.97, 1.77, and 1.61. The observations suggest that a volume holographic nanograting forms within sample type III. The thickness of this nanograting is comparable to the wavelength of the incident laser beam. It's noteworthy that the effective refractive indices for sample type III are notably higher than those of the other two samples.

In both Figures 5(b) and 5(c), the symmetric curved scattering patterns observed around the central line are attributed to the emergence of intricate gratings in both sample types II and III. These patterns arise due to the superimposition of two or three individual gratings with varying line-spaces, leading to the creation of a complex grating, as previously reported [22]. Fig. 6 provides a schematic representation, elucidating the formation of these complex gratings in samples type II and III.

The grating vector for waves propagating in a complex grating adheres to the phase-matching condition [9]:

$$\vec{k}_0 + l\vec{G} = \vec{k}_s, \tag{15}$$

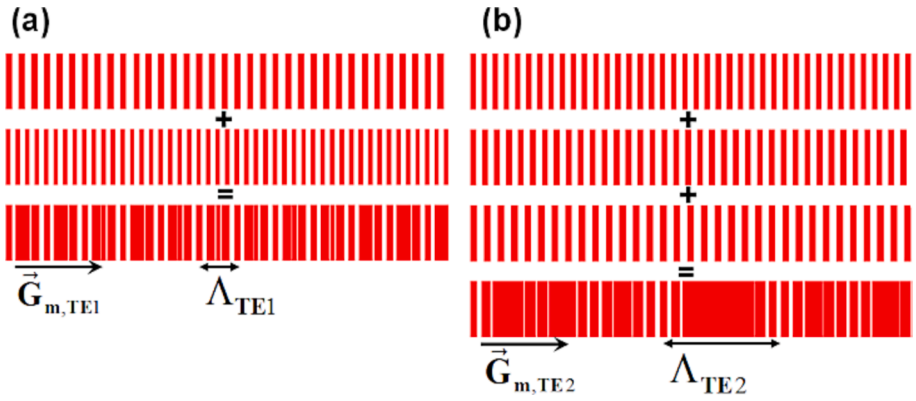

Fig. 6. Schematic representation illustrating the formation of complex gratings in (a) type II and (b) type III samples.

where $\vec{k}_o$ represents the incident wave vector, $\vec{k}_s$ is the scattered wave vector, $\vec{G}_l$ denotes the grating vector, and l is the diffraction order. As demonstrated in Fig. 6, the grating vector is oriented perpendicular to the grating lines. The magnitude of the grating vector is given by $G_l = 2\pi/\Lambda$, with Λ representing the periodicity of the complex grating.

Given the normal incident irradiation depicted in Fig. 3, there's no component of the incident wave in the direction of the grating vector ($k_{0,x} = 0$). The x-component of the scattered wave vector can be expressed as $k_{s,x} = 2\pi\sin\theta_s/\lambda_0$, where θ_s is the diffraction angle depicted in Fig. 3. This leads to the phase-matching condition in the x-axis direction [19,23]:

$$\frac{l\lambda_0}{\Lambda} = \sin\theta_s. \tag{16}$$

According to equation (16), for a diffraction pattern to manifest on the screen in Fig. 3, the periodicity of the complex grating (Λ) must exceed the wavelength of the incident light ($\Lambda > l\,\lambda_0$). Fig. 6 indicates that the period of a complex grating can surpass that of each individual simple grating. Specifically, the period of the complex grating in sample type II (Λ_{TE1}), resulting from the superposition of two simple gratings with line-spaces of 310 nm and 345 nm, is roughly 1 μm. Consequently, the periodicity of sample type II exceeds the incident wavelength $\lambda_0 = 532$ nm, yet remains below $2\lambda_0$. Thus, only the first-order diffraction ($l = 1$) is visible in Figure 5(b). For the complex grating in sample type III (Λ_{TE2}), its period is approximately 3.5 μm, which is less than $7\lambda_0$. Hence, diffraction patterns ranging from the first to the sixth order can be observed on the screen, as shown in Figure 5(c).

3.2. Linear dichroism in silver nanogratings

Fig. 7(a), 7(b), and 7(c) depict the optical density for sample types I, II, and III, respectively. Notably, the AgCl film is mostly transparent in visible light. The emergence of absorption peaks in the spectra is attributed to the localized surface plasmon resonance (LSPR) of the silver nanoparticles [24,15]. The broad optical density peaks in the spectra for types I, II, and III result from a diverse size distribution of these nanoparticles [25].

In the optical density spectra of Ag-AgCl samples, readings obtained using a perpendicular polarized probe beam ($OD_\perp$) are consistently higher than those gathered using a parallel polarized probe beam ($OD_\parallel$). Specifically, the spectrum of sample type I features two LSPR peaks: the first at 470 nm and the second at 580 nm. These peaks confirm the formation of an anisotropic nanostructure in the samples [26]. Meanwhile, the spectra for samples type II and type III exhibit a distinctive shoulder at 450 nm, coupled with a broad LSPR peak at 610 nm.

Referencing Fig. 7, the LSPR peaks within the spectra for samples type I, type II, and type III are located at wavelengths 500 nm, 515 nm, and 520 nm, respectively. The migration of the LSPR peak towards a

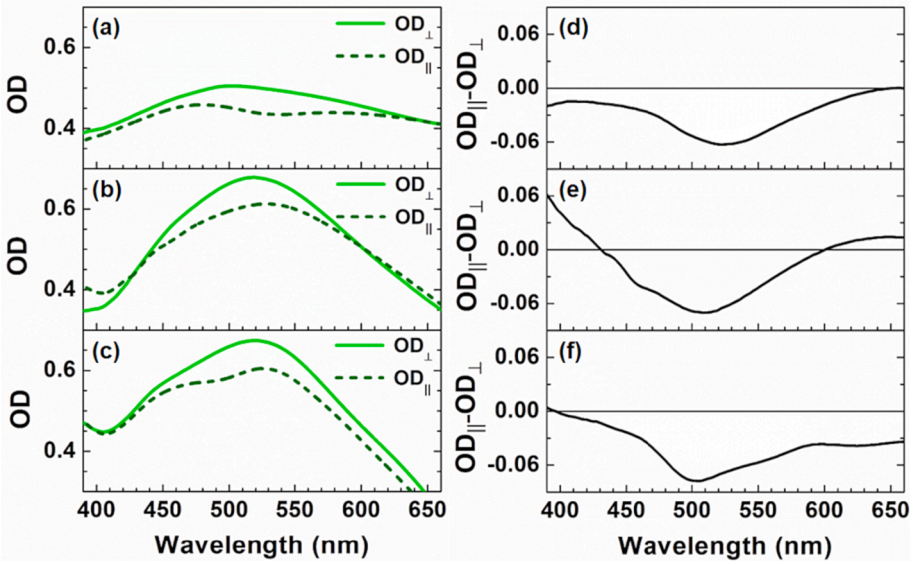

Fig. 7. The figure illustrates the optical density spectra for samples (a) type I, (b) type II, and (c) type III. Additionally, the linear dichroism spectra for each sample type are provided in (d) type I, (e) type II, and (f) type III.

longer wavelength is attributed to the increased effective refractive index surrounding the silver nanogratings, encompassing the glass substrate, AgCl thin film, and overlying air layer [27].

Turning our attention to the linear dichroism spectra, these are displayed for sample types I, II, and III in Fig. 7(d), 7(e), and 7(f) respectively. Linear dichroism, in this context, behaves as a wavelength-sensitive parameter in an anisotropic plasmonic medium [12,25]. In the case of sample type I, the most significant linear dichroism value aligns closely with the incident laser wavelength ($\lambda_0 = 532$ nm). This observation indicates that this sample effectively captures the wavelength of the incident laser beam [4,5,15]. In contrast, the peak values of linear dichroism for samples type II and type III are pegged at wavelengths of 510 nm and 505 nm, respectively. This suggests that the surface holographic nanograting in sample type I more accurately registers the wavelength information of the incoming wave compared to the volume holographic nanogratings in samples type II and type III.

3.3. Optical rotation

Optical rotation measurements were conducted for samples of types I, II, and III using an experimental arrangement as illustrated in Fig. 8. For these measurements, we employed a probe beam with a wavelength of 532 nm—the wavelength at which these samples typically exhibit their peak linear dichroism values. To ensure the silver nanogratings within the samples remained unaffected during testing, the probe beam's intensity was moderated using a neutral density (ND) filter. Before the beam was allowed to traverse the sample, it was polarized vertically using a polarizer.

When no sample is present, and both the polarizer and analyzer are positioned crosswise, the detector registers no light. Introducing a sample between these two components causes the sample to induce a rotation in the light wave's polarization azimuth. To gauge this rotation, the analyzer must be adjusted until the light's intensity reaches its minimum value. The degree to which the analyzer is rotated provides a measure of the optical rotation. For our experiments, optical rotation angles were determined for various sample orientation angles, ranging from $\Phi = 0^\circ$ to $\Phi = 180^\circ$, with increments of 15°.

Fig. 9(a), 9(b), and 9(c) graphically represent the optical rotation angles measured against the sample orientation for samples type I, type II, and type III, respectively. Across all the Ag-AgCl sample types, the optical rotation values were observed to be roughly zero at orientation angles $\Phi = 0^\circ$, 90°, and 180°. This suggests that the probe beam's polarization exiting the sample remains largely unaffected. Consequently, this implies that the sample's fast and slow axes align either parallel or perpendicular to the nanograting lines. Notably, at orientation angles of $\Phi = 45^\circ$ and 135°, the optical rotation reaches its peak absolute value.

The experimental data shown in Fig. 9 can be fit using Equation (12), as depicted by the dashed line. For the surface holographic nanograting in sample type I, the amplitude of the sine function (A_0) – a measure of linear dichroism – is $A_0 = 3.1^\circ \pm 0.3^\circ$. However, for the volume holographic nanogratings in sample types II and III, the amplitudes are found to be $A_0 = 10.7^\circ \pm 0.3^\circ$ and $A_0 = 11.7^\circ \pm 0.3^\circ$ respectively. It should be noted that holographic nanogratings are promising candidates for the design of polarized-sensitive photodetectors and waveplates [28,29].

Although the AgCl film thickness in samples type II and type III is five and ten times greater than in sample type I, the measured A_0 for samples type II and type III are only three and four times greater than that of sample type I. It was anticipated that A_0 in Ag-AgCl samples would rise linearly with the increased thickness of the AgCl film. The observed deviation is attributed to the interference among various plasmonic modes in samples type II and III. This interference results in light scattering depolarization at a wavelength of 532 nm, leading to a decrease in A_0 [25].

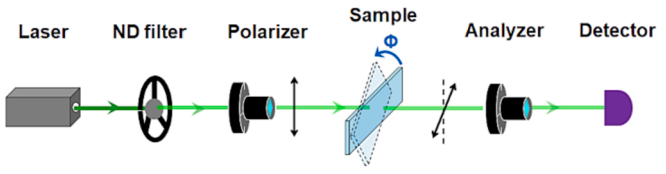

Fig. 8. Schematic representation of the experimental setup employed for optical rotation measurements.

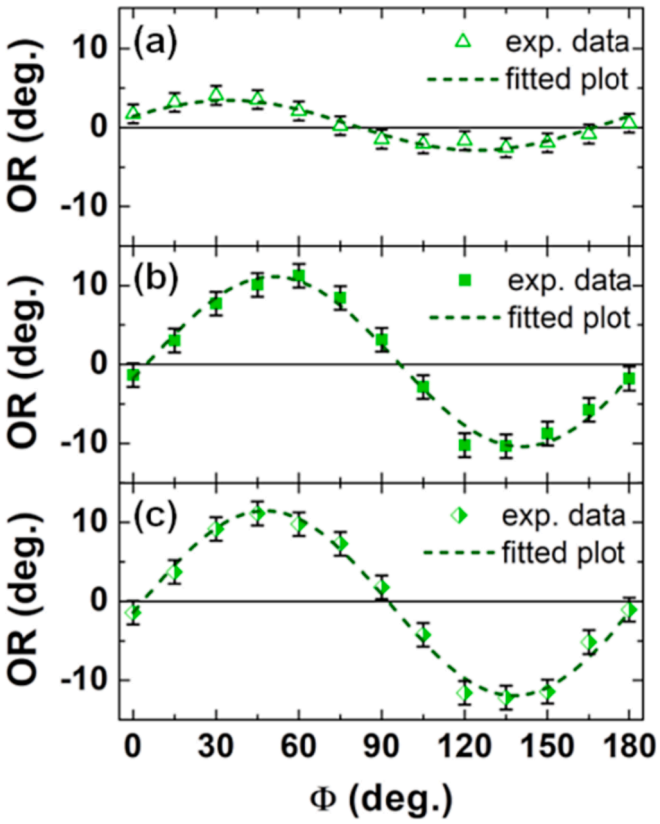

Fig. 9. Optical rotation measurements for Ag-AgCl samples across various orientations: (a) type I, (b) type II, and (c) type III.

3.4. Birefringence

Birefringence in the Ag-AgCl film can be discerned by evaluating the ellipticity angles (η) of the probe beam traversing the Ag-AgCl film [7,12]. To achieve this, a polarimeter is incorporated into the setup depicted in Fig. 8, taking the place of the analyzer and detector. Fig. 10 (a), 10(b), and 10(c) display the ellipticity angles, measured as functions of the sample orientation, for samples type I, type II, and type III, respectively. The peak birefringence value for silver nanogratings in the AgCl thin film is recorded at a wavelength of 632.8 nm; thus, a probe beam of this wavelength is employed for measuring ellipticity [7,12].

For the sample types I, II, and III, the values of induced birefringence are 0.29, 0.10, and 0.02 respectively. The maximum birefringence is observed for sample type I, which consists of a surface holographic nanograting. The emergence of intricate nanogratings in samples type II and III leads to a substantial reduction in birefringence.

Birefringence in plasmonic anisotropic materials arises due to the phase retardance between transverse and longitudinal plasmonic resonances [30]. When the transverse plasmonic resonance surpasses its longitudinal counterpart, there is a positive phase retardation, and the reverse holds true [30]. As detailed in section 3.1, samples type II and III consist of complex gratings formed by the overlay of two and three simple gratings with different line-spacing, respectively. This layering likely causes the observed reduced birefringence in these samples,

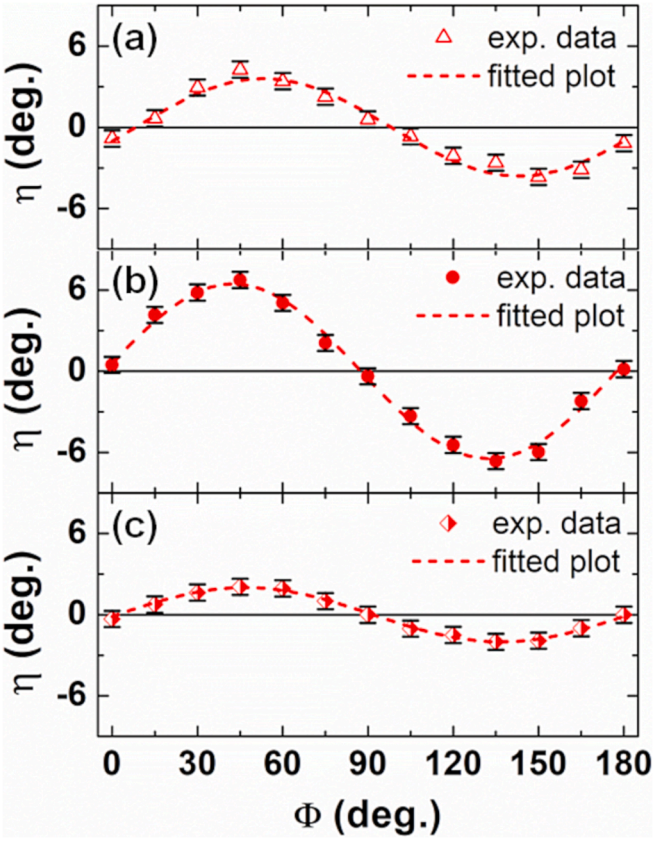

Fig. 10. Ellipticity measurements at varying orientations of Ag-AgCl samples for (a) type I, (b) type II, and (c) type III.

stemming from the superposition of simple gratings each exhibiting a distinct birefringence direction. Interestingly, despite this reduced birefringence, linear dichroism remains relatively strong when compared to sample type I. Materials showing such pronounced dichroism find potential applications in devices like nanophotonic switches and modulators [29].

4. Conclusion

In this study, we elucidated the process of forming both surface and volume holographic silver nanogratings within an AgCl waveguide. Notably, the volume holographic nanogratings are crafted via the interference between the incident laser beam and higher-order TE modes present in the AgCl waveguide. A distinctive aspect of our method for creating volume holographic silver nanogratings in the AgCl film is the use of a single low-power laser beam. Furthermore, we circumvented the need for specialized couplers to introduce laser beams into the AgCl waveguide. Another advantage is the ability to monitor the quality of the volume holographic nanograting during laser exposure by observing the scattering and diffraction patterns displayed on a screen. These holographic silver nanogratings, both surface and volume types, act as anisotropic media and exhibit noteworthy optical characteristics, including linear dichroism and birefringence. The localized surface plasmon resonance (LSPR) of the periodic silver nanostructures enables the recording of wavelength information in these plasmonic nanostructures. Consequently, the linear dichroism of the holographic silver nanograting emerges as a wavelength-dependent feature. The utmost absolute value of linear dichroism is discerned near the incident laser's wavelength. It's also evident that sample type I, embedded with surface holographic nanogratings, more accurately registers the wavelength of the incident laser beam. Additionally, sample type I manifests the highest birefringence value. In summary, the propagation of elevated-order TE modes in the AgCl waveguide culminates in the emergence of intricate nanogratings. It's also noteworthy that the birefringence induced in such a configuration is considerably diminished compared to an AgCl film solely propagating the TE_0 mode, where a surface silver nanograting is generated.

Declaration of competing interest

The authors declare the following financial interests/personal relationships which may be considered as potential competing interests: [Daryoosh Vashaee reports financial support was provided by National Science Foundation (NSF). Daryoosh Vashaee reports a relationship with National Science Foundation (NSF) that includes: funding grants].

Data availability

No data was used for the research described in the article.

Acknowledgement

This research was partially funded by the National Science Foundation (NSF) under grant number CBET-2110603.

References

[1] L.A. Ageev, V.K. Miloslavsky, Photoinduced effects in light-sensitive films, Opt. Eng. 34 (1995) 960.
[2] T. Tamir, Integrated optics, Springer, Berlin, 1979.
[3] A. Nahal, R. Talebi, Ellipticity-dependent laser-induced optical gyrotropy in AgCl thin films doped by silver nanoparticles, J. Nanopart. Res. 16 (6) (2014) 1–12.
[4] R. Talebi, A. Nahal, M.Y. Bashouti, S.H. Christiansen, Optical nanostructuring in light-sensitive AgCl-Ag waveguide thin films: Wavelength effect, Opt. Express 22 (2014) 30669–30682.
[5] L.A. Ageev, V.K. Miloslavsky, A. Nahal, Holographic recording of visible-light spectra in thin AgCl-Ag waveguide films, J. Opt. A Pure Appl. Opt. 1 (2) (1999) 173–177.
[6] V.K. Miloslavsky, A. Nahal, L.A. Ageev, Peculiarities of spontaneous gratings formation in photosensitive films under linearly and circularly polarization radiation, Opt. Commun. 147 (4–6) (1998) 436–442.
[7] S.S. Jazi, R. Talebi, Manipulating birefringence in AgCl thin film loaded by silver nanoparticles under normal and oblique incident angles, J. Phys. D 53 (2019), 015303.
[8] A. Nahal, B. Asaakareh, M. Miri, Temporal evolution of photoinduced optical chirality in nanostructured light-sensitive waveguide thin films: Simultaneous excitation of TE0 and TE1 modes, J. Appl. Phys. 125 (2019), 123101.
[9] Y. Lim, H. Park, B. Kang, K. Kim, D. Yang, S. Lee, Holography, fourier optics, and beyond photonic crystals: holographic fabrications for weyl points, bound states in the continuum, and exceptional points, Adv. Photonics Res. 2 (2021) 2100061.
[10] Y. Tomita, T. Aoi, S. Hasegawa, F. Xia, Y. Wang, J. Oshima, Very high contrast volume holographic gratings recorded in photopolymerizable nanocomposite materials, Opt. Express 28 (2020) 14.
[11] A. Liu, Y. Zhang, Y. Weng, Z. Shen, B. Wang, Diffraction efficiency distribution of output grating in holographic waveguide display system, IEEE Photon. J. 10 (2018) 4.
[12] R. Talebi, F.T. Ghahfarokhi, D. Vashaee, Photoinduced tunable birefringence and dichroism in silver nanogratings, J. Opt. Soc. Am. B 37 (10) (2020) 2848–2855.
[13] M. Kotha, A. Kaloyeros, T. Murray, S. Gallis, Wavelength-dependent anisotropic optical properties in layered GaTe for polarization-sensitive applications, Adv. Photonics Res. 2 (2021) 2100140.
[14] S. Murai, T. Tsujiguchi, K. Fujita, K. Tanaka, Enhanced form birefringence of metal nanoparticles with anisotropic shell mediated by localized surface plasmon resonance, Opt. Express 19 (2011) 23.
[15] R. Talebi, Investigating multicolour photochromic behaviour of AgCl and AgI thin films loaded with silver nanoparticles, Phys. Chem. Chem. Phys. 20 (2018) 5734.
[16] A. Matikainen, T. Nuutinen, P. Vahimaa, S. Honkanen, A solution to the fabrication and tarnishing problems of surface-enhanced Raman spectroscopy (SERS) fiber probes, Sci. Rep. 5 (2015) 8320.
[17] C. An, S. Wang, Y. Sun, Q. Zhang, J. Zhang, C. Wang, J. Fang, Plasmonic silver incorporated silver halides for efficient photocatalysis, J. Mater. Chem. A 4 (2016) 4336–4352.
[18] C. Bohren, D. Huffman, Absorption and scattering of light by small particles, John Wiley & Sons, New York, 1983.
[19] R. Talebi, S. Izadi, Investigating surface morphology of Ag-AgCl thin film by scattering pattern at normal and oblique incident angles, Appl. Opt. 57 (2018) 10355–10363.
[20] G.Q. Wallace, S.T. Read, D.M. McRae, S.M. Rosendahl, F. Lagugné-Labarthet, Exploiting anisotropy of plasmonic nanostructures with polarization modulation

infrared linear dichroism microscopy (μPM-IRLD), Adv. Optical Mater. 6 (6) (2018) 1701336.
[21] Y.P. Svirko, N.i. Zheludev, *Polarization of light in nonlinear* optics, John Wiley & Sons, New York, 1998.
[22] Z.M. Zhang, L.P. Wang, Measurements and modeling of the spectral and directional radiative properties of micro/nanostructured materials, Int. J. Thermophys. 34 (2013) 2209–2242.
[23] A. Guglielmelli, S.H. Nemati, A.E. Vasdekis, L.D. Sio, Stimuli responsive diffraction gratings in soft-composite materials, J. Phys. d: Appl. Phys. 52 (2019), 053001.
[24] M. Choi, K. Shin, J. Jang, Plasmonic photocatalytic system using silver chloride/silver nanostructures under visible light, Adv. Colloid Interface Sci. 341 (2010) 83.
[25] S. Requena, H. Doan, S. Raut, A. D'Achille, Z. Gryczynski, I. Gryczynski, Y. M. Strzhemechny, Linear dichroism and optical anisotropy of silver nanoprisms in polymer films, Nanotechnology 27 (2016), 325704.
[26] V.V. Shinde, P.R. Jadhav, J.H. Kim, P.S. Patil, One-step synthesis and characterization of anisotropic silver nanoparticles: application for enhanced antibacterial activity of natural fabric, J. Mater. Sci. 48 (2013) 8393–8401.
[27] A.D. McFarland, R.P.V. Duyne, Single silver nanoparticles as real-time optical sensors with zeptomole sensitivity, Nano Lett. 3 (8) (2003) 1057–1062.
[28] S. Yang, C. Hu, M. Wu, W. Shen, S. Tongay, K. Wu, B. Wei, Z. Sun, C. Jiang, L. Huang, Z. Wang, In-plane optical anisotropy and linear dichroism in low-symmetry layered TlSe, ACS Nano 12 (8) (2018) 8798–8807.
[29] S.H. Suk, S. Nah, M. Sajjad, S.B. Seo, J. Song, N. Singh, S. Sim, Polarization-driven ultrafast optical switching in TiS3 nanoribbons via anisotropic hot carrier dynamics, Adv. Optical Mater. 11 (2023) 2300370.
[30] Y. Jen, W. Liu, M. Cong, T. Chan, Bideposited silver nanocolloid arrays with strong plasmon-induced birefringence for SERS application, Sci. Rep. 10 (2020) 20143.